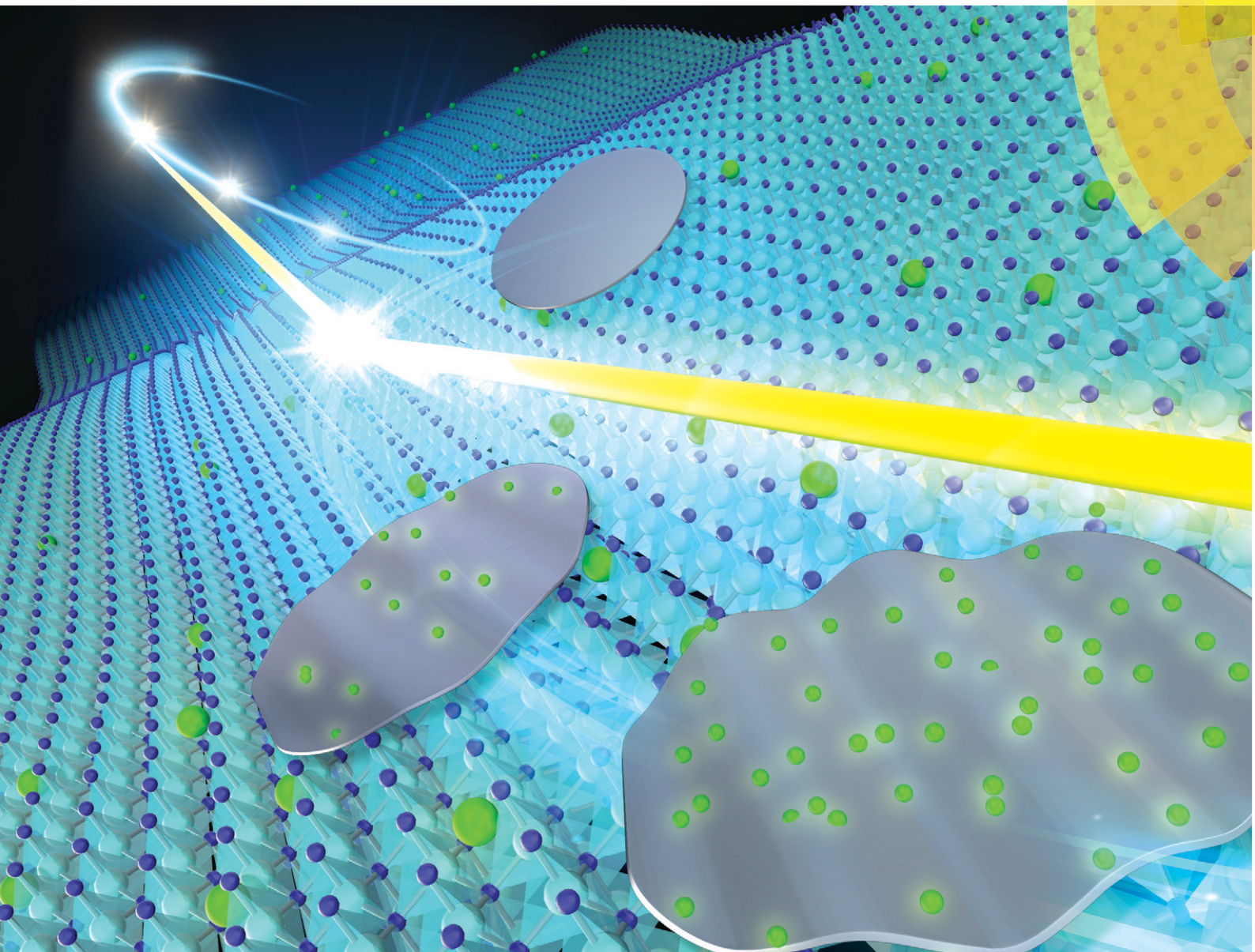


CrystEngComm

rsc.li/crystengcomm



ISSN 1466-8033



ROYAL SOCIETY
OF CHEMISTRY

Celebrating
IYPT 2019

PAPER

Osami Sakata *et al.*

Lattice-plane bending angle modulation of Mg-doped GaN homoepitaxial layer observed by X-ray diffraction topography



Cite this: *CrystEngComm*, 2019, 21, 2281

Lattice-plane bending angle modulation of Mg-doped GaN homoepitaxial layer observed by X-ray diffraction topography

Jaemyung Kim,^{ab} Okkyun Seo,^{abc} Chulho Song,^{†b} Satoshi Hiroi,^{bc} Yanna Chen,^{†bc} Yoshihiro Irokawa,^a Toshihide Nabatame,^a Yasuo Koide^a and Osami Sakata^{†*abc}

We have studied the lattice-plane modulation of Mg-doped GaN homoepitaxial layers by X-ray diffraction topography. X-ray rocking curve images and full-width at half maxima images of a 2 inch GaN wafer were obtained by an image stacking method. Low frequency components evaluated from Fourier transformations of the X-ray rocking curves tended to increase as the Mg-doping concentration increased, which indicates an increase of film lattice modulation. For Mg-dopant concentrations greater than 10^{19} cm^{-3} , the film lattice-plane changed from a convex to concave shape and became wrinkled. We attribute this lattice-plane modulation to the relaxation of strain in the in-plane direction after the generation of dislocations by Mg doping.

Received 7th November 2018,
Accepted 4th February 2019

DOI: 10.1039/c8ce01906a

rsc.li/crystengcomm

Introduction

A recently developed hydride vapour phase epitaxy (HVPE) method has enabled the growth of large and high-quality GaN wafers.^{1,2} Homo-epitaxial layers grown on this GaN substrate show the highest crystallinity available in industry.^{3,4} However, for applications to optoelectronics^{5,6} and power devices,^{7,8} control of the dopant concentration is a critical factor. After electron beam irradiation and thermal annealing, Mg-doped GaN shows a considerable increase of photoluminescence (PL) efficiency.^{5,6} Although a Mg and hydrogen assisted model has been proposed to explain the increase of the PL efficiency, the actual mechanism of the increase remains a topic of debate.⁹ Mg-Doping to GaN increases the lattice parameters in both the *a* and *c* directions, but the lattice constant variations are very small.¹⁰ In the case of Si-doped GaN, sometimes, it shows strain, dislocations, and even cracks in its films, which deteriorate the GaN crystal quality.¹¹ However, the microscale information obtained to date is not

appropriate for understanding how these effects influence the overall wafer on a macroscopic scale such as HRTEM (high-resolution transmission electron microscopy)¹² or EELS (electron energy loss spectroscopy).¹³ A better understanding of the wafer scale origins is needed to overcome these side effects and enable mass production of GaN wafers.

Although X-ray rocking curves are widely used to observe GaN crystallinity, this technique only gives local rather than global information. Thus, conventional rocking curve measurements are not suitable for evaluating the crystallinity of the whole wafer. To overcome this issue, X-ray rocking curves have been combined with scanning methods based on motorized sample stages.^{1,14} However, these approaches do not fully cover the whole wafer owing to time and cost limitations.

In the case of an X-ray diffraction topography technique based on the Berg-Barrett method,^{15–21} it has provided us with wafer scale information such as the dislocation distribution. This method is suitable for crystalline materials rather than layered materials because 2D materials have Bragg rods instead of Bragg points in the reciprocal space.²² Recently developed lattice-plane orientation mapping shows the importance of wafer scale imaging for understanding wafer bending and crystallinity distribution over 2 and 4 inch GaN wafers.^{20,21}

Here we show the effects of Mg doping on GaN homoepitaxial layers over a wafer by X-ray diffraction topography methods. We applied Fourier analysis of the bending angle line profiles to reveal an increase of the bending angle

^a Center for GaN Characterization, Research Network and Facility Services Division (RNFS), National Institute for Materials Science (NIMS), Tsukuba, Ibaraki, 305-0047 Japan. E-mail: SAKATA.Osami@nims.go.jp

^b Synchrotron X-ray Group, Research Center for Advanced Measurement and Characterization, NIMS, Kouto, Sayo, Hyogo, 679-5148 Japan

^c Synchrotron X-ray Station at SPring-8, RNFS, NIMS, Kouto, Sayo, Hyogo, 679-5148 Japan

[†] Current address: NISSAN ARC, LTD., 1 Natsushima-cho, Yokosuka, Kanagawa, 237-0061 Japan.



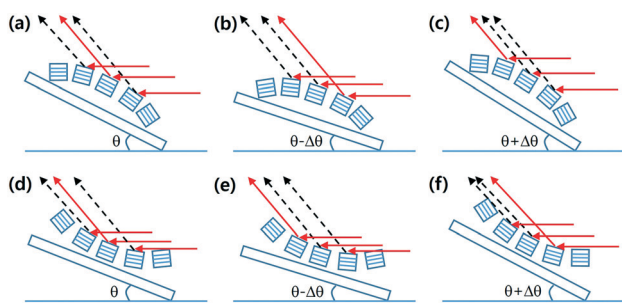


Fig. 1 X-ray diffraction configurations in concave (a–c) and convex (d–f) lattice-planes illustrated at various incident angles. The diffracted X-rays are those emitted from lattice-planes that satisfy the Bragg condition.

modulation as the Mg concentration increased owing to strain relaxation in the in-plane directions.

Experimental details

The samples were 2 μm -thick Mg-doped GaN layers with Mg-dopant concentrations of 10^{17} , 10^{18} , and 10^{19} cm^{-3} grown on a 1 μm -thick undoped GaN layer on a 330 μm -thick GaN (0001) 2 inch wafer as the substrate. The concentrations of Mg in the GaN layers were estimated using a calibration curve of Mg dopant concentrations, which were obtained from analysis of secondary ion mass spectroscopy depth profiles of reference samples, as a function of Cp_2Mg (bis cyclopentadienyl magnesium) supply amounts, and had a standard deviation of 10%. The X-ray diffraction topography experiments were performed at BL20B2 SPring-8, Japan. An X-ray wavelength of 1.284 \AA was selected with a Si (111) double crystal monochromator having a size of 100 mm (h) \times 1.5 mm (v), which was large enough to fully cover the 2 inch

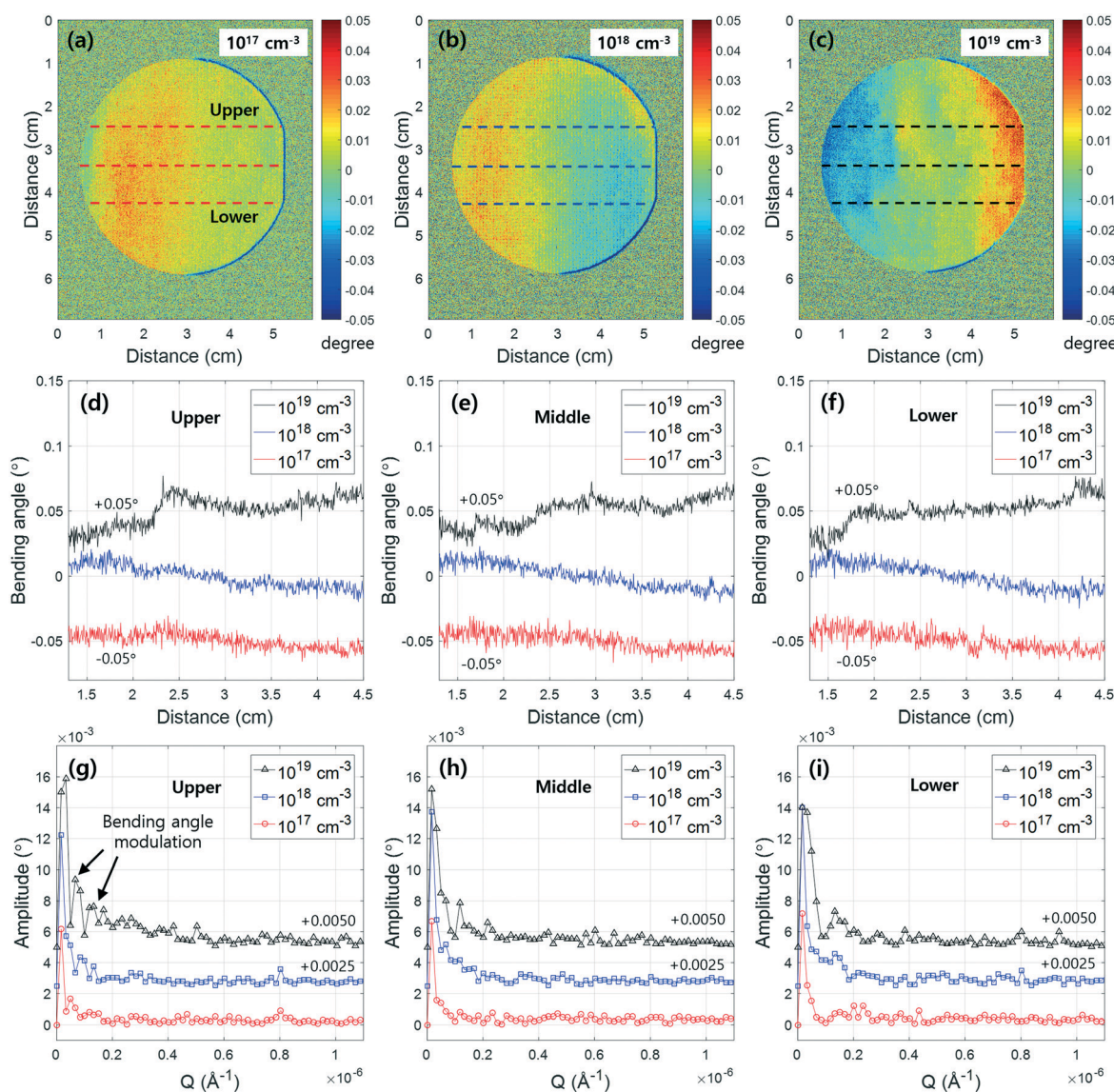


Fig. 2 Merged 2 inch GaN images at various Mg doping concentrations are illustrated in (a)–(c). The intensities in the image represent the bending angles evaluated from the partially diffracted X-ray images at respective pixel positions. Line profiles representing the wafer bending at the top, center, and lower parts are shown in (d)–(f). Fourier transformation results of these line profiles are shown in (g), (h), and (i), respectively. Low frequency components related to the lattice modulation dominate at an Mg concentration of 10^{19} cm^{-3} .



wafer. A flat panel detector (C7942, Hamamatsu Photonics) with a pixel size of $50 \times 50 \mu\text{m}^2$ was installed for image acquisition. The incident angle was adjusted to be 0.58° , which satisfied the GaN (11 $\bar{2}$ 4) Bragg condition. We obtained partially diffracted images at various incident angles and evaluated the rocking curve images by an image stacking technique.^{20,21} In the case of a bent crystal, the positions that satisfied the Bragg condition diffracted X-rays. Six of the available diffraction configurations in the bent crystal are illustrated in Fig. 1(a)–(f). For a convex shape, the diffraction position moved to the right, when irradiated with X-rays from right to the left, as shown in Fig. 1(b). Conversely, if we increased the incident angle, the diffraction position moved to the left, as shown in Fig. 1(c). If the lattice-plane has a concave shape, the situation was reversed, as shown in Fig. 1(d)–(f). Through this X-ray diffraction technique, we obtained bending angle information on the lattice-plane.

Results and discussion

The bending angle maps at Mg concentrations of 10^{17} , 10^{18} , and 10^{19} cm^{-3} are shown in Fig. 2(a)–(c), respectively. The intensity patterns indicate the bending angles evaluated from the rocking curves at the respective detector pixel position. At Mg concentrations of 10^{17} and 10^{18} cm^{-3} , the bending angle changed monotonously. However, at 10^{19} cm^{-3} , modulation of the bending angles in the vicinity of the central parts was clearly seen. The overall bending angle envelope changed from a concave to convex shape. Both the envelope changes of the bending angles and film wrinkling are shown by the changes of the bending angle envelopes [Fig. 2(c)]. To understand the change of the bending angle quantitatively, we selected specific line profiles of each wafer, as shown in Fig. 2(d)–(f). The bending angles obtained from the upper sides of each wafer are shown in Fig. 2(d). For Mg concentrations of 10^{17} and 10^{18} cm^{-3} , the overall values were shifted by $\pm 0.05^\circ$. However, in the case of the highest doping concentration of 10^{19} cm^{-3} , abrupt increases and decreases of the bending angles were observed, which implies the existence of lattice-plane modulation at high Mg concentrations. This situation was similar for the center and lower parts of the samples, as shown in Fig. 2(e) and (h). To determine the frequency components from the bending angle modulation, we applied Fourier transformations to the obtained line profiles. The calculated frequency components of the upper, middle, and lower parts are shown in Fig. 2(g)–(i), respectively. In the case of the upper region, the increase of the low frequency components strongly affected the bending angle fluctuation, as shown in Fig. 2(g). In the case of a Mg-doping concentration of 10^{19} cm^{-3} , the dominant frequency was $0.67 \times 10^{-6} \text{ \AA}^{-1}$ with a corresponding modulation period of approximately 9.4 mm. Another strong frequency component at $0.13 \times 10^{-6} \text{ \AA}^{-1}$ with a 4.7 mm modulation period was also observed. These two strong frequency components mainly contributed to the wafer bending and wrinkling of the GaN films.

To understand the relationship between the amplitude obtained from Fourier transformation and the Mg concentration, we calculated the amplitude summation of Fig. 2(g)–(i), which can be used to represent the film modulation, as shown in Fig. 3(a). As the Mg concentration increased, the total amplitude increased. The trend was similar for the wafer upper, center, and lower parts. The mean values at a Mg-doping concentration of 10^{19} cm^{-3} were approximately two times as high as those at 10^{17} cm^{-3} . We interpret this result as indicating that the high Mg doping of the GaN homoepitaxial layers increased the stress in the in-plane direction of the film. As shown in Fig. 3(b), the films had low bending at the initial stage. As the Mg concentration increased, the lattice-plane bending angle increased. At Mg concentrations greater than 10^{19} cm^{-3} , the increase of stress enabled relaxation by film wrinkling. According to a report on stress relaxation¹⁸ of Si-doped GaN observed by Raman spectroscopy,^{11,24} an increase of the Si doping concentration induces stress relaxation of the films and the dislocation density increases. In this respect, our observation is similar to the previous report, which was based on a Si dopant.¹¹ To confirm our model proposed in Fig. 3(b), we evaluated the full-width at half maxima (FWHM) maps by an image stacking method, as illustrated in

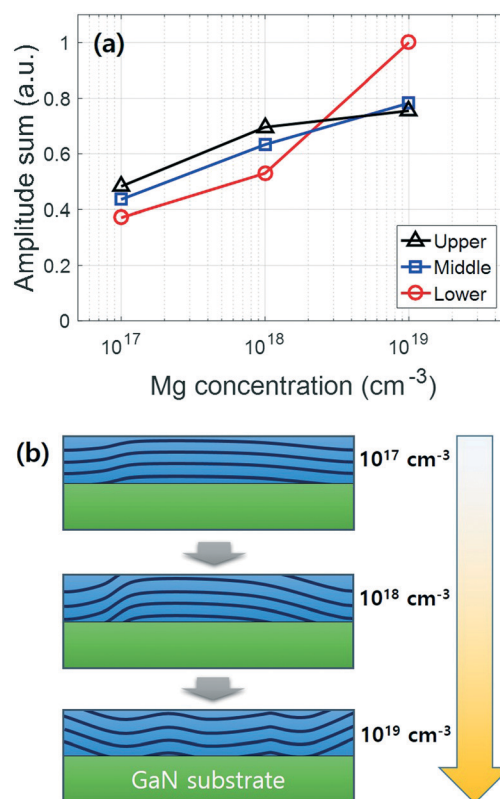


Fig. 3 Amplitude summation evaluated from Fourier transformation is represented in (a). The evaluated values were proportional to the Mg concentration. The proposed Mg-induced lattice bending model is shown in (b). As the Mg dopant concentration increased, the lattice bending angle increased up to a Mg concentration of 10^{18} cm^{-3} . At higher concentrations, the films became wrinkled and changed from a convex to concave shape.



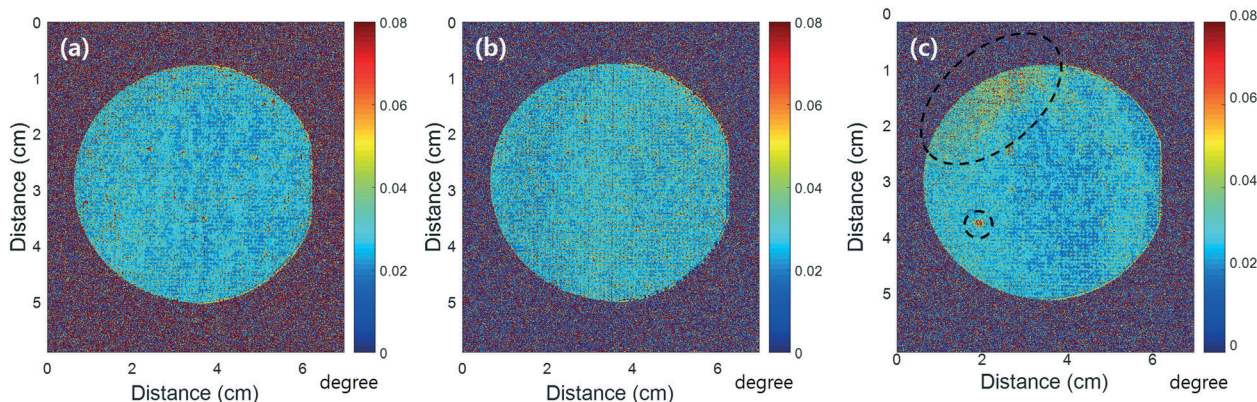


Fig. 4 FWHM maps of Mg concentrations of 10^{17} (a), 10^{18} (b), and 10^{19} cm^{-3} (c) evaluated from the image stacking method are described. As the Mg concentration increased, the FWHM increased owing to the increase of mosaicity induced by Mg atoms. The dashed circle area indicates a region of high mosaicity.

Fig. 4(a)–(c). The color scale indicates the FWHM angle. For a Mg concentration of 10^{17} cm^{-3} , the FWHM showed a homogeneous distribution. For a Mg concentration of 10^{18} cm^{-3} , we observed an increase of the FWHM in the middle of the wafer. At a Mg concentration of 10^{19} cm^{-3} , the edge parts inside the circles showed a particularly large FWHM, which indicated an increase of the mosaicity of GaN (11 $\bar{2}$ 4) domains. The increase of the FWHM in the vicinity of the wafer edge in Fig. 4(c) is the result of compressive stress relaxation in the in-plane direction if the substrates used have similar lattice-plane bending distributions. The origin of a small point-like area, having a large FWHM value within the circle in Fig. 4(c), cannot be explained without stress relaxation. This assumption is consistent with a previously mentioned report.²³ The increase of FWHM is related to an increase of mosaicity or dislocation density.

According to previous reports, the dislocation density can be directly calculated from the rocking curve width broadening and the length of the Burgers vector.^{25,26} For the rocking curve obtained at the GaN (11 $\bar{2}$ 4) peak, the broadening provides the threading dislocation (TD) density. However, the best way to observe dislocations is to use transmission electron microscopy (TEM) with atomic resolution²⁷ or atomic force microscopy (AFM) of a clean surface.^{29,30} Without measurements at this resolution, it is difficult to evaluate the dislocation density and the length of the Burgers vector. A recently developed two-photon excitation photoluminescence technique²⁸ has also shown dislocation images in 3D. However, the spatial resolution of this method is insufficient to distinguish dislocations smaller than 300 nm. In some cases, a formula developed by Kaganer²⁶ is useful for estimating the dislocation density. However, according to Barchuk *et al.*, X-ray rocking curves can show the same features even at very different dislocation densities.³¹ They interpreted the broadening of rocking curves through wafer bowing and misorientation from a macroscopic viewpoint. From a microstructural point of view, they associated the rocking curve broadening with the dislocation density. They revealed that dislocation densities obtained from Monte Carlo simulations

were strongly dependent on the model even with the same rocking curve. For these reasons, careful attention should be paid to interpreting dislocation densities based on X-ray rocking curves.

Conclusions

In conclusion, we have observed the lattice-plane bending angle modulations of GaN homoepitaxial layers by X-ray diffraction topography. As the Mg concentration increased, the bending angles increased and the film became wrinkled. At an Mg concentration of 10^{19} cm^{-3} , the envelope of the lattice-plane changed from a concave to convex shape. Fourier transformations of the bending angle line profiles obtained from X-ray diffraction topography images showed an increase of low frequency components as the doping concentration increased. The evaluated low frequency components with periods of 9.4 and 4.7 mm was dominant under the highest doping concentration. The envelope of the overall lattice-planes became convex and wrinkled at high Mg concentrations. The increase of the FWHM at the wafer edge implies that stress relaxation occurs with an increase of dislocation density at high Mg concentrations.

Conflicts of interest

There are no conflicts to declare.

Acknowledgements

The measurements were performed at SPring-8 under proposals No. 2016B1028, 2017A1030, 2017B1029, 2017B1030, 2018B1010, 2017B4505, and 2018B4505. This work was supported by the Ministry of Education, Culture, Sports, Science and Technology (MEXT) “Program for Research and Development of Next-Generation Semiconductor to Realize Energy-Saving Society”. We thank Andrew Jackson, PhD, from Edanz Group (www.edanzediting.com/ac) for editing a draft of this manuscript.



Notes and references

- 1 R. Dwiliński, R. Doradziński, J. Garczyński, L. P. Sierzputowski, A. Puchalski, Y. Kanbara, K. Yagi, H. Minakuchi and H. Hayashi, *J. Cryst. Growth*, 2008, **310**, 3911–3916.
- 2 K. Fujito, S. Kubo, H. Nagaoka, T. Mochizuki, H. Namita and S. Nagao, *J. Cryst. Growth*, 2009, **311**, 3011–3014.
- 3 M. Lee, D. Mikulík, M. Yang and S. Park, *CrystEngComm*, 2017, **19**, 2036–2041.
- 4 T. Kimura, K. Horibuchi, K. Kataoka and D. Nakamura, *J. Cryst. Growth*, 2018, **494**, 17–25.
- 5 S. Nakamura, T. Mukai, M. Senoh and N. Iwasa, *Jpn. J. Appl. Phys.*, 1992, **31**, L139–L142.
- 6 H. Amano, M. Kito, K. Hiramatsu and I. Akasaki, *Jpn. J. Appl. Phys.*, 1989, **28**, L2112–L2114.
- 7 Y. Wu, D. Kapolnek, J. P. Ibbetson, P. Parikh, B. P. Keller and U. K. Mishra, *IEEE Trans. Electron Devices*, 2001, **48**, 586–590.
- 8 W. Saito, Y. Takada, M. Kuraguchi, K. Tsuda, I. Omura, T. Ogura and H. Ohashi, *IEEE Trans. Electron Devices*, 2003, 2528–2531.
- 9 J. L. Lyons, A. Janotti and C. G. Van de Walle, *Phys. Rev. Lett.*, 2012, **108**, 156403.
- 10 P. Prystawko, M. Leszczynski, B. Beaumont, P. Gibart, E. Frayssinet, W. Knap, P. Wisniewski, M. Bockowski, T. Suski and S. Porowski, *Phys. Status Solidi B*, 1998, **210**, 437–443.
- 11 L. T. Romano, C. G. Van de Walle, J. W. Ager, W. Götz and R. S. Kern, *J. Appl. Phys.*, 2000, **87**, 7745–7752.
- 12 S. D. Lester, F. A. Ponce, M. G. Craford and D. A. Steigerwald, *Appl. Phys. Lett.*, 1995, **66**, 1249–1251.
- 13 I. Arslan and N. D. Browning, *Phys. Rev. Lett.*, 2003, **91**, 165501.
- 14 Y. Cui, X. Hu, X. Xie, R. Wang and X. Xu, *CrystEngComm*, 2017, **19**, 3844–3849.
- 15 J. Chaudhuri, M. H. Ng, D. D. Koleske, A. E. Wickenden and R. L. Henry, *Mater. Sci. Eng., B*, 1999, **64**, 99–106.
- 16 X. Xu, R. P. Vaudo, C. Loria, A. Salant, G. R. Brandes and J. Chaudhuri, *J. Cryst. Growth*, 2002, **246**, 223–229.
- 17 B. Raghathamachar, G. Dhanaraj, J. Bai and M. Dudley, *Microsc. Res. Tech.*, 2006, **69**, 343–358.
- 18 K. Barla, G. Bomchil, R. Herino, J. C. Pfister and J. Baruchel, *J. Cryst. Growth*, 1984, **68**, 721–726.
- 19 D. Lübbert, C. Ferrari, P. Mikulík, P. Pernot, L. Helfen, N. Verdi, D. Korytár and T. Baumbach, *J. Appl. Crystallogr.*, 2005, **38**, 91–96.
- 20 J. Kim, O. Seo, C. Song, S. Hiroi, Y. Chen, Y. Irokawa, T. Nabatame, Y. Koide and O. Sakata, *Appl. Phys. Express*, 2018, **11**, 081002.
- 21 J. Kim, O. Seo, C. Song, Y. Chen, S. Hiroi, Y. Irokawa, T. Nabatame, Y. Koide and O. Sakata, *CrystEngComm*, 2018, **20**, 7761–7765.
- 22 J. Als-Nielsen and D. McMorrow, *Elements of Modern X-Ray Physics*, New York, 2001.
- 23 C. Kisielowski, J. Krüger, S. Ruvimov, T. Suski, J. W. Ager, E. Jones, Z. Liliental-Weber, M. Rubin, E. R. Weber, M. D. Bremser and R. F. Davis, *Phys. Rev. B: Condens. Matter Mater. Phys.*, 1996, **54**, 17745–17753.
- 24 I. Lee, I. Choi, C. Lee, E. Shin, D. Kim, S. Noh, S. Son, K. Lim and H. Lee, *J. Appl. Phys.*, 1998, **83**, 5787–5791.
- 25 B. Heying, X. H. Wu, S. Keller, Y. Li, D. Kapolnek, B. P. Keller, S. P. DenBaars and J. S. Speck, *Appl. Phys. Lett.*, 1996, **68**, 643–645.
- 26 V. M. Kaganer, O. Brandt, A. Trampert and K. H. Ploog, *Phys. Rev. B: Condens. Matter Mater. Phys.*, 2005, **72**, 045423.
- 27 C. Chen, C. Zhu, E. R. White, C. Chiu, M. C. Scott, B. C. Regan, L. D. Marks, Y. Huang and J. Miao, *Nature*, 2013, **496**, 74–77.
- 28 T. Tanikawa, K. Ohnishi, M. Kanoh, T. Mukai and T. Matsuoka, *Appl. Phys. Express*, 2018, **11**, 031004.
- 29 A. M. Walker, B. Slater, J. D. Gale and K. Wright, *Nat. Mater.*, 2004, **3**, 715–720.
- 30 S. Dumrul, S. Bazzana, J. Warzywoda, R. R. Biederman and A. Sacco Jr., *Microporous Mesoporous Mater.*, 2002, **54**, 79–88.
- 31 M. Barchuk, V. Holý and D. Rafaja, *J. Appl. Phys.*, 2018, **123**, 161552.

